Dalton Transactions

ROYAL SOCIETY OF CHEMISTRY

PAPER

View Article Online
View Journal | View Issue



Cite this: *Dalton Trans.*, 2024, **53**, 18515

# Single-ion magnetism in novel Btp-based cobalt complexes of different charge†

Gustavo Rama-Martínez, ‡[a] Marcelo Osorio-Celis, ‡[a] Yolanda Sabater-Algarra, ‡[a] Diego Sánchez-Brunete,[a] Antonio L. Llamas-Saiz,[c] Eugenia P. Quirós-Díez,[a] M. Eugenio Vázquez,[b] Miguel Vázquez López[a] and María del Carmen Giménez López *[a]

The magnetic behavior of single-ion metal complexes may be influenced by the nature and composition of the secondary coordination sphere that can be composed of solvent molecules and counterions bound through non-covalent interactions. However, achieving precise control over the outer-coordination sphere of these magnetic complexes to demonstrate its influence on their magnetic properties presents a challenge. A strategy for varying the number of counterions, while simultaneously preserving the arrangement of the ligand atoms around the metal center without altering its oxidation state, is to adjust the overall formal charge of the complex. This adjustment could lead to changes in the magnetic properties of single-ion metal complexes. In this study, we present two novel ligands featuring the coordinating unit Btp (2,6-bis(1,2,3-triazol-4-yl)pyridine). These ligands are equipped with functional groups that can potentially undergo deprotonation. By carefully selecting the solvents used during the crystallization process of the complexes, we can tune at will the charge of the complexes, thus modifying the composition of the $Co^{II}$ complexes' outer-coordination sphere. We show that, by modifying these conditions, we can tailor the secondary coordination sphere of both charged (mono- and dicationic) and neutral anisotropic $Co^{II}$ metal complexes to show field-induced single-ion magnetism, influencing in turn the size of the barrier to reversal of the magnetization and their slow relaxation process.

Received 16th August 2024,
Accepted 3rd October 2024

DOI: 10.1039/d4dt02338b

rsc.li/dalton



## Introduction

3d single-ion magnets (SIMs) are a sub-class of monometallic single-molecule magnets in which the magnetic properties of these compounds originate from a single ion within a ligand field.[1] These systems have attracted increasing attention over the last twenty years for their potential applications in high-density data storage,[2] quantum computing[3] and spintronics.[4] Although lanthanide ions have been the focus of most of the research in this area,[5] 3d transition metal complexes are another major paramagnetic source for the construction of SIMs.[6]

Magnetic properties of these SIMs depend mainly on the d-orbital splitting, which in turn depends on various factors related to the metal ion (*i.e.*, its oxidation state and the principal quantum number of its d-valence orbitals), the nature of the coordinated ligand(s), or the geometry around the metal ion, among others. So far most of the 3d metal complexes reported displaying SIM behavior exhibit several shared characteristics for their first coordination sphere, including low coordination numbers and reduced geometries that may be induced through bulky groups, as well as an efficient quantum tunneling of the magnetization (QTM) in the absence of an applied direct current (dc) field.[7]

The outer-sphere, or secondary coordination sphere, of a metal ion refers to any molecule—mainly from the solvent(s)—or counterions that interact with the metal complex through supramolecular forces.[8] It is known that these outer-sphere interactions can affect the metal-binding properties of the ligand(s) and can even cause structural distortions in the metal complex, thus affecting its reactivity[9] and some of its properties such as, for example, those related to magnetism.[10]

[a]*Centro Singular de Investigación en Química Biolóxica e Materiais Moleculares (CiQUS) and Departamento de Química Inorgánica, Universidade de Santiago de Compostela, 15782 Santiago de Compostela, Spain. E-mail: maria.gimenez.lopez@usc.es*
[b]*Centro Singular de Investigación en Química Biolóxica e Materiais Moleculares (CiQUS) and Departamento de Química Orgánica, Universidade de Santiago de Compostela, 15782 Santiago de Compostela, Spain*
[c]*Unidade de Raios X. Área de Infraestruturas de Investigación, Universidade de Santiago de Compostela, 15782 Santiago de Compostela, Spain*

†Electronic supplementary information (ESI) available: Experimental details, supplementary tables, and figures. CCDC 2281061, 2281065 and 2281066. For ESI and crystallographic data in CIF or other electronic format see DOI: https://doi.org/10.1039/d4dt02338b

‡These authors contributed equally to this work.

In this context, although the properties of SIMs are essentially based on discrete molecules, the metal complexes in single crystals are not isolated, but are part of a highly organized superstructure together with solvent molecules and counterions, where every interaction counts for the final magnetic behavior of the system as a whole. The importance of the secondary coordination sphere in SIMs has been described previously.[11,12] However, the development of methods to control these external interactions in a magnetic context is still a relatively unexplored matter.[13]

In this work we report the synthesis of two new 2,6-bis(1,2,3-triazol-4-yl)pyridine (Btp) ligands. This ligand is broadly studied in other chemical disciplines, in fact this scaffold has been studied in spin crossover magnetic systems.[14–16] However, no reported literature was found for systems based in other metals suitable for SIM behavior. As well as the synthesis of $^{tBuOOC}$**Btp** and $^{HOOC}$**Btp** (Scheme 1), here we report the X-ray crystal structures and the magnetic properties of a serie of anisotropic $Co^{II}$ complexes derived from these ligands exhibiting field-induced single-ion magnetism: $[Co(^{tBuOOC}\mathbf{Btp})_2](ClO_4)_2$ (**1**), $[Co(^{HOOC}\mathbf{Btp})(^{OOC}\mathbf{Btp})]_2(ClO_4)_2\cdot 6H_2O$ (**2**), $[Co(^{OOC}\mathbf{Btp})_2]\cdot CH_3CN\cdot 3H_2O$ (**3**).

We discuss here how the precise selection of terminal functionalizations of the tridentate metal-binding motif, combined with the appropriate choice of solvents during the crystallization process, allows for the tuning of the formal charge of the anisotropic complex, while preserving the arrangement of ligand atoms around the metal center without altering the metal oxidation state. Consequently, this approach adjusts the composition of the outer coordination sphere of $Co^{II}$ complexes in single crystals, which could influence the size of the barrier to reversal of magnetization and their slow relaxation process.

The study and understanding of these structural differences would aid in comprehending the variances observed in the magnetic behavior of the compounds. Thus, we will endeavor to establish correlations and/or trends between structural parameters, such as single ion anisotropy and orbital splitting, among other factors. Understanding these relationships may shed light on the modulation of energy barriers and the mechanisms underlying slow relaxation of the magnetization.[17,18]

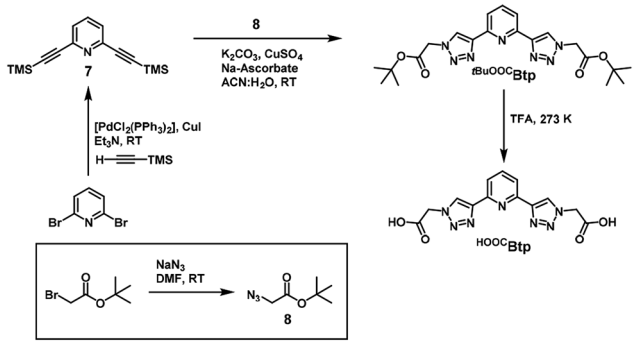


**Scheme 1** Synthetic scheme of the ligands $^{tBuOOC}$**Btp** and $^{HOOC}$**Btp**.

## Results and discussion

### Synthesis of the Btp ligands

Btp derivatives are a class of terdentate ligands with high versatility in terms of functionalization and metal-binding properties,[19] and that have been widely used in coordination[20] and supramolecular chemistry,[21] including applications in magnetochemistry.[16] Since they contain triazole units in their structure, which are generated by click chemistry (CuAAC), they are considered members of the "click ligands" or "clickates".[15]

Two novel Btp ligands, named $^{tBuOOC}$**Btp** and $^{HOOC}$**Btp**, were synthesized here by CuAAC methods (Scheme 1). The former is equipped with two *tert*-butyl acetate terminal arms, whereas the latter is the corresponding acetic acid analog. Both ligands were obtained pure and characterized by reversed phase ultra-high performance liquid chromatography (RP-UHPLC), electrospray ionization mass spectrometry (ESI-MS), and $^1$H- and $^{13}$C-NMR spectroscopy (see ESI, Fig. S1–S13†).

### Preparation of $Co^{II}$ complexes derived from the Btp ligands

By using UV-vis and fluorescence spectroscopy, the formation constants of the $Co^{II}$ complexes with $^{tBuOOC}$**Btp** and $^{HOOC}$**Btp** were studied in solution. As shown in the ESI (Fig. S14–S18†), all data sets were processed to extract the corresponding titration profiles and fitted using the DynaFit software,[22] which has been extensively used to calculate the formation constants of classic coordination compounds and other complex systems, such as metallopeptides.[23,24] The titration profiles, obtained through both spectroscopic techniques, were successfully fitted to a 1 : 2 (M : L) binding model using DynaFit.[18] The values obtained for the global association constants calculated from both spectroscopic techniques for the homoleptic compounds with $^{tBuOOC}$**Btp** and $^{HOOC}$**Btp** are very similar, and only slightly smaller in comparison with other cobalt complexes with terdentate ligands reported in the literature demonstrating a strong metal–ligand interaction (Table 1).[25,26]

Considering the data obtained from UV-vis and fluorescence, the formation of the cobalt complexes with varying charges (ranging from dicationic to neutral) were prepared in

**Table 1** Values of the stepwise association constants ($K_1$ and $K_2$) calculated for UV-vis and fluorescence titrations in $CH_3OH$ for a binding model 1 : 2 (M : L). The global formation constants ($\beta_2$) were calculated by the equation $\beta_2 = K_1 \cdot K_2$; where $K_1$ and $K_2$ are the stepwise formation constants

| | UV-vis | | | Fluorescence | | |
|---|---|---|---|---|---|---|
| | $\log K_1$ | $\log K_2$ | $\log \beta_2$ | $\log K_1$ | $\log K_2$ | $\log\beta_2$ |
| $Co^{II}$ *vs.* $^{tBuOOC}$**Btp** | 3.96 | 3.91 | 7.87 ± 0.04 | 4.00 | 3.99 | 7.99 ± 0.04 |
| $Co^{II}$ *vs.* $^{HOOC}$**Btp** | 3.96 | 3.69 | 7.65 ± 0.07 | 3.99 | 3.79 | 7.78 ± 0.07 |

solution by mixing a $Co^{II}$ perchlorate salt with the corresponding ligand ($^{tBuOOC}$**Btp** and $^{HOOC}$**Btp**) in a 1 : 2 ratio. After allowing the resulting solution to slowly evaporate at room temperature under a constant flow of nitrogen, single crystals suitable for X-ray diffraction studies were collected. When a 1 : 1 mixture of $CH_3OH/CH_3CN$ was used as the solvent medium, clear orange single crystals of the homoleptic $Co^{II}$ complex derived from $^{tBuOOC}$**Btp** of formula $[Co(^{tBuOOC}\mathbf{Btp})_2](ClO_4)_2$ (**1**) were collected. It is worth noting that both the formula and the structure depicted for **1** in Fig. 1 do not include solvent information. The crystallographic data of **1** indicate the presence of molecules of solvent in the crystal structure (one cavity filled with solvent with a volume of 354 $Å^3$ per unit cell), which is further supported by the gradual weight loss below 100 °C observed from the thermogravimetric measurements (Fig. S19a†). However, attempts to model the disordered solvent were unsuccessful. The SQUEEZE procedure from the PLATON program was used to account for the contribution of the disordered molecules' electron density to the measured experimental crystal diffraction data.[27] Within the cavity, we identified a total of 73 electrons, which corresponds to an approximate maximum occupancy of 4 methanol molecules, which agrees with elemental analysis performed on the crystals of **1**. Therefore, as a reasonable approximation, we assumed that the crystallographic asymmetric unit of the void (half of the total cavity volume) might contain 2 methanol molecules an the crystal stoichiometry is $C_{42}H_{54}CoN_{14}O_8$, 2 $(ClO_4)$, 2$(CH_4O)$ (Table S1†).

We have observed that by choosing the crystallization solvent and in presence of the divalent metal ion, we can deprotonate the carboxylic groups of $^{HOOC}$**Btp** coordinating the metal, tuning the formal charge of the resulting metal complexes. Thus, using a low-deprotonating solvent mixture ($CH_3OH/CH_3CN$ in a 1 : 1 ratio), clear light orange single crystals of a monocationic $Co^{II}$ complex of formula $[Co(^{HOOC}\mathbf{Btp})(^{OOC}\mathbf{Btp})]_2(ClO_4)_2{\cdot}6H_2O$ (**2**) were obtained, in which only one of the $^{HOOC}$**Btp** ligands in the complex is monodeprotonated (referred to as $^{OOC}$**Btp**). By using a more strongly-deprotonating solvent mixture ($CH_3CN : H_2O$ in a 1 : 1 ratio), translucent orange single crystals of the neutral homoleptic $Co^{II}$ complex of formula $[Co(^{OOC}\mathbf{Btp})_2]{\cdot}CH_3CN{\cdot}3H_2O$ (**3**) were isolated with both $^{HOOC}$Btp ligands monodeprotonated.

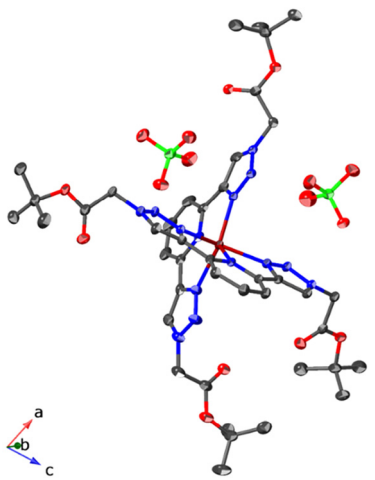


**Fig. 1** Thermal ellipsoids (30% probability ellipsoids) representation for the crystal structure of $[Co(^{tBuOOC}\mathbf{Btp})_2](ClO_4)_2$ (**1**) without the contribution of the disordered solvent. X-Ray crystal diffraction data can be found in the ESI.† Hydrogens and disordered atoms have been omitted for clarity. Carbon is represented in grey, nitrogen in blue, oxygen in red, chlorine in light green, and cobalt in brown.

Thermogravimetric analysis (TGA) was performed on the collected single crystals of the obtained $Co^{II}$ complexes under dry air in the range of 40–1000 °C with a scan rate of 2 °C $min^{-1}$ (Fig. S19†). The gradual weight loss observed below 110 °C for all the compounds agrees with the presence of solvated molecules ascertained by X-ray single-crystal diffraction. After desolvation, the weight loss with increasing temperature for compounds **2** and **3** occurs in three consecutive steps, while compound **1** shows an additional weight loss step at 180 °C, involving the loss of the *tert*-butyl groups. After 250 °C all the compounds exhibit a weight loss corresponding to the thermal decomposition of $ClO_4^-$ anions and the carboxylic groups. The complete decomposition of the Btp ligands to yield $Co_2O_3$ takes place in two consecutive steps between 300–550 °C for **1**, 300–500 °C for **2**, and 300–450 °C for **3**. The solid residue isolated at 1000 °C corresponds to $Co_3O_4$.

### Crystal structures of Btp derived $Co^{II}$ complexes

Single-crystal X-ray diffraction was used to determine the structures of the compound **1–3** at 100 K, all of which crystallize in the triclinic space group $P\bar{1}$ (Table S1†). The asymmetric unit cell for compounds **1** and **3** contains only one $Co^{II}$ metal center, while two crystallographically independent $Co^{II}$ centers are found for compound **2**. In all cases, the $Co^{II}$ metal centers are coordinated by two Btp ligand units, resulting in a pseudo-octahedral $CoN_6$ coordination environment around the metal ion (Fig. 1–3). The Co–N bond distances found for all the complexes (2.0933(14)–2.1811(16) Å for **1**, 2.072(5)–2.184(16) Å for **2** and 2.0913(14)–2.1637(16) Å for **3**) are above 2 Å and typical of $Co^{II}$ centres in high spin (Scheme S1 and Table S2†).[28] The deviation of the $CoN_6$ coordination environment from a regular octahedral geometry is expected to influence the magnetic properties of the metal complexes. This deviation becomes evident when analyzing the distortion indices $\Sigma$ and $\Theta$ for the $Co^{II}$ complexes (**1–3**). $\Sigma$ measures the deviation of a metal ion from an ideal octahedral geometry considering the sum of the deviation of the 12 *cis* N–Co–N angles from 90°, while $\Theta$ indicates its distortion from an octahedral towards a trigonal prismatic structure as the sum of the 24 N–Co–N angles measured on the projection of two triangular faces of the octahedron along their common pseudo-threefold axis (Scheme S2†). Both indices were obtained using the OctaDist program[29] and their values deviate significantly from $\Sigma = \Theta =$ 0, which would indicate a perfect octahedral geometry (Table S3†).[30,31] The deviation of $CoN_6$ from a regular octahedral coordination geometry can also be observed by examining the $N_{triazole}$–Co–$N_{triazole}$ angles within each of the co-

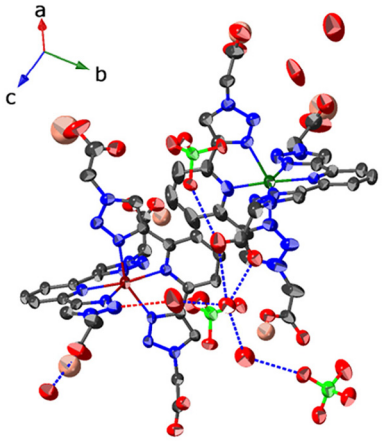


**Fig. 2** Thermal ellipsoids (30% probability ellipsoids) representation for the crystal structure of [Co($^{HOOC}$**Btp**)($^{OOC}$**Btp**)]$_2$(ClO$_4$)$_2$·6H$_2$O (**2**). The asymmetric unit contains two metal complexes that interact through π–π stacking interactions between the pyridine rings. X-Ray crystal diffraction data can be found in the ESI.† Hydrogen bonds between oxygen atoms are depicted as blue dashed lines and between oxygen and nitrogen atoms in red dashed lines. Hydrogens are omitted for clarity, except for the carboxylic groups, and the disordered atoms are also omitted, except for one perchlorate, which has an occupancy factor of 0.5. Carbon is represented in grey, nitrogen in blue, oxygen in red, chorine in light green, cobalt in brown (Co1) and green (Co2) and hydrogen in pink.

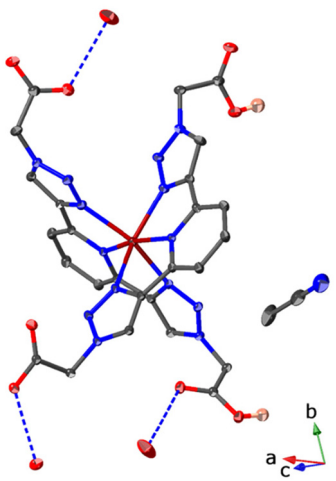


**Fig. 3** Thermal ellipsoids (30% probability ellipsoids) representation for the crystal structure of [Co($^{OOC}$**Btp**)$_2$]·CH$_3$CN·3H$_2$O (**3**). X-Ray crystal diffraction data can be found in the ESI.† Hydrogens are omitted for clarity, except for the carboxylic groups and the disordered atoms are also omitted. Hydrogen bonds between oxygen atoms are depicted as blue dashed lines. Carbon is represented in grey, nitrogen in blue, oxygen in red and cobalt in brown.

ordinated ligands, as well as the $N_{pyridine}$–Co–$N_{pyridine}$ angle involving the two coordinated ligands. These angles deviate significantly from the ideal 180° symmetry (parameter $\Psi$ (ranging from 152.18(4)–150.15(6)°) and $\varphi$ (ranging from 166.35(7)–173.22(1)°)), respectively (Scheme S3 and Table S3†). We also observed for **1–3** a deviation from 90°, expected for a perfect octahedral environment, for the dihedral angle between the planes containing the atoms of the $^{tBuOOC}$**Btp** and $^{HOOC}$**Btp** ligands coordinating the metal (parameter $\theta$ in Table S3†). By the careful analysis of all these parameters for the Co$^{II}$ complexes (**1–3**), a strongly distorted octahedral geometry can be inferred.

Although all the compounds **1–3** contain solvated molecules, the designed Co$^{II}$ complexes do not interact with the solvent in the same way. It is evident that compound **1** is more hydrophobic compared to compounds **2** and **3**. This difference is attributed to the inability of the $^{tBuOOC}$**Btp** ligand to form strong, directional hydrogen bonds with the solvent molecules (Fig. 1). Consequently, it can be inferred that the influence of the solvent on complex **1** is very limited, and its magnetic properties are likely to remain unaffected by the presence of the solvent.

In contrast, $^{HOOC}$**Btp** is equipped with two carboxylic acids that can provide hydrogen-bonding sites for solvent molecules in the molecular packing. When the mixture used in the crystallization is CH$_3$CN/CH$_3$OH 1 : 1, only one of the carboxylic acids in one of the two $^{HOOC}$**Btp** units of the metal complex is deprotonated, giving rise to the monocationic metal complex ion **2**, which contains one perchlorate counterion in their second coordination sphere (Fig. 2). However, when CH$_3$CN/H$_2$O in 1 : 1 ratio is used in the crystallization process, two carboxyl groups, one from each of the $^{HOOC}$**Btp** units are deprotonated, resulting in the formation of the neutral complex **3** (Fig. 3). In the $^{HOOC}$**Btp**-derived complexes, hydrogen bonds are formed between water molecules in the second coordination sphere and the carboxylic groups (protonated or not) of the ligands (see Fig. 1–3). Interestingly, the presence of water molecules is a constant element in both $^{HOOC}$**Btp**-derived complexes (**2** and **3**), regardless of whether water was used in the medium mixture for crystallization. Thus, it is hypothesized that the presence of water in the crystals can be attributed to the use of both undried organic solvents (CH$_3$OH and CH$_3$CN) and hydrated metal salts. Nevertheless, the presence of stronger secondary interactions (H-bonds) in **2** and **3** may have a stronger influence on the relaxation processes.

Regarding the role of the $ClO_4^-$ counterions in the second coordination sphere of the metal complexes (Fig. 1 and 2), the obvious difference is the number of perchlorates between the dicationic (**1**) and the monocationic (**2**) complex. For the former, the interaction is solely through non-directional electrostatic interactions, while for the latest, the interaction with the protonated acid group of the metal complexes can be established through a direct (O–H···O$_{Cl}$) or a water mediated (O–H$_{COOH}$···O$_{Cl}$···H–O$_{COOH}$) hydrogen bonding (Fig. 2 and Table S4†).

In the crystal packing, the Co$^{II}$ complexes are arranged in either cationic or neutral layers for **1–2** and **3**, respectively, where the shortest Co–Co distances are found (7.63(6) Å for **1**, 7.79(1) Å for **2** and 7.31(1) Å for **3**) with interlayer Co–Co separations ranging from 11.04(1) Å for **2** to 13.97(8) Å for **1** (Table S6†). For **1**, the [Co($^{tBuOOC}$**Btp**)$_2$]$^{2+}$cationic layers are stacked along the *a*-axis *via* van der Waals forces between the

*tert*-butyl arms of the **Btp** ligands (Fig. 4). Within the layer, the $[Co(^{tBuOOC}\mathbf{Btp})_2]^{2+}$ complexes are interacting by pyridine–pyridine and pyridine–triazole π–π interactions along the *b*-axis (Table S7†). The analysis of π–π interactions for all three compounds has been conducted taking into account the distance between centroids, the dihedral angle between the planes containing the centroids, and the slippage. Here, we have taken into consideration distances up to 4.0 Å, angles below 20°, and minimized slippages.[32] The growth of the cationic layer along the *c* direction is facilitated *via* van der Waals forces between the *tert*-butyl arms. The $ClO_4^-$ anions fill the interstitial spaces in the structure (Fig. S20†). For compound **2**, the cationic layers are stacked along the *a*-axis through hydrogen bonding involving the water molecules, the $ClO_4^-$ anions and the carboxylic groups (Fig. 5 and Fig. S21, Table S4†). Within the layer, the two crystallographic independent $[Co(^{HOOC}\mathbf{Btp})(^{OOC}\mathbf{Btp})]^+$ complexes interact by π–π interactions along *c*-axis and hydrogen bonding involving $ClO_4^-$ anions and the carboxylic groups from the Btp units along *b*-axis (Fig. S21 and Table S8†). For compound **3**, the $[Co(^{OOC}\mathbf{Btp})_2]$ neutral layers are stacked along the *b*-axis, connected through hydrogen bond *via* the water molecules present in the second coordination sphere ($O_{COOH}\cdots H\text{–}O_w\text{–}H\cdots O_{COOH}$) (Fig. 6 and Table S5†). Within the layers, the $[Co(^{OOC}\mathbf{Btp})_2]$ complexes are connected by π–π interactions between pyridine–pyridine and pyridine–triazole groups of the Btp ligands along both the *a* and *c*-axis (Table S9†).

## Magnetic studies

**Static magnetic studies.** Direct-current (dc) magnetic measurements were performed on a collection of ground single crystals for all the complexes (**1–3**) (Fig. S22†). The $\chi_M T$ values for the $Co^{II}$ complexes at 300 K (3.45 emu K $mol^{-1}$ for **1**, 6.02 emu K $mol^{-1}$ for **2** and 3.69 emu K $mol^{-1}$ for **3**) are larger than the "spin-only" $\chi_M T$ values calculated for one (1.87 emu K $mol^{-1}$) and two (3.74 emu K $mol^{-1}$) non-interacting high-spin $Co^{II}$ ions ($t_{2g}^5\ e_g^2$, $S = 3/2$, $g = 2.0$) per formula (as expected from the obtained crystallographic $Co^{II}$–N bond distances, Table S2†). These large $\chi_M T$ values usually indicate the existence of an unquenched orbital angular momentum contribut-

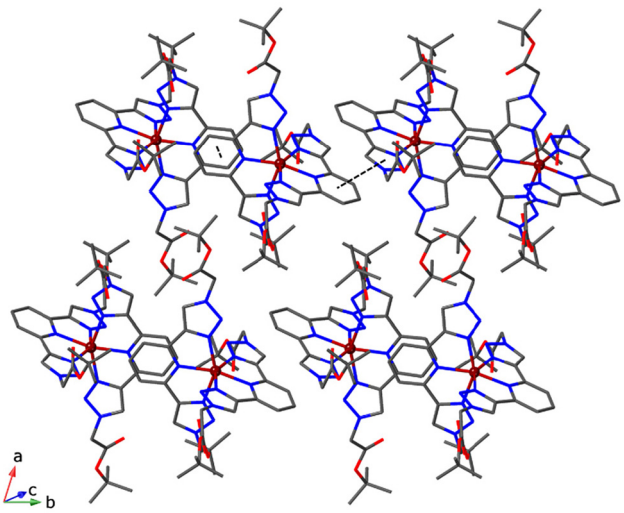


**Fig. 4** Ball and stick representation of the cationic layers of the $Co^{II}$ complexes stacked along the *a*-axis in the crystal packing of $[Co(^{tBuOOC}\mathbf{Btp})_2](ClO_4)_2$ (**1**). Hydrogens and anions are omitted for clarity. π–π interactions are highlighted using black dashed lines. Carbons are in grey, nitrogen in blue, oxygen in red and cobalt in dark brown.

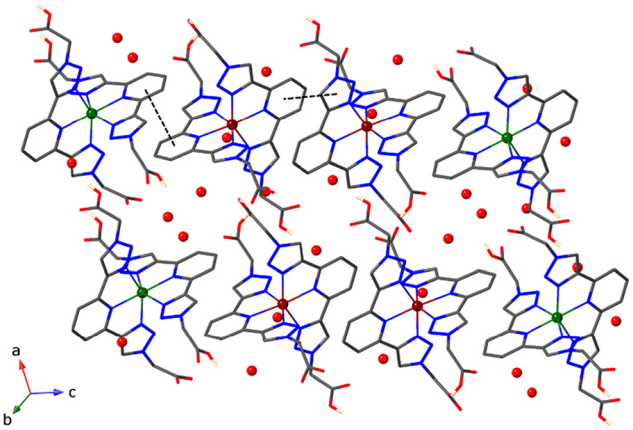


**Fig. 5** Ball and stick representation of the cationic layers of the $Co^{II}$ complexes growing along the *c*-axis in the crystal packing of $[Co(^{HOOC}\mathbf{Btp})(^{OOC}\mathbf{Btp})]_2(ClO_4)_2{\cdot}6H_2O$ (**2**). Hydrogens and anions are omitted for clarity, except for the hydrogens of the carboxylic acids. π–π interactions are highlighted using black dashed lines. Carbons are in grey, nitrogen in blue, oxygen in red, hydrogen in pink and cobalt in green and dark brown. Water molecules are represented using red spheres.

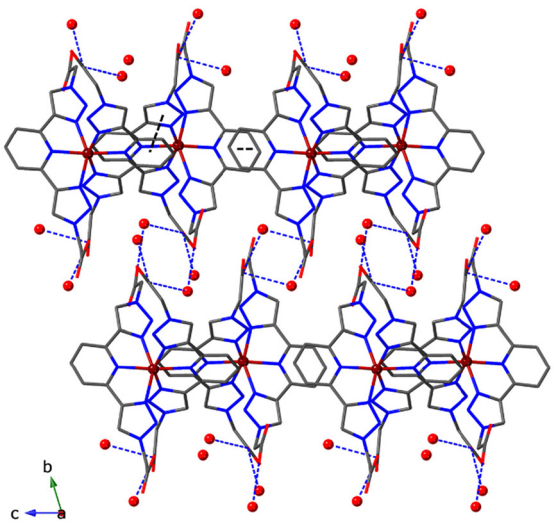


**Fig. 6** Ball and stick representation of the cationic layers of the $Co^{II}$ complexes stacked along the *b*-axis in the crystal packing of $[Co(^{OOC}\mathbf{Btp})_2]{\cdot}CH_3CN{\cdot}3H_2O$ (**3**). Hydrogens are omitted for clarity. π–π interactions are highlighted using black dashed lines and H-bonds with blue dashed lines. Carbons are in grey, nitrogen in blue, oxygen in red and cobalt in dark brown. Oxygen atoms of the water molecules are depicted as red spheres.

ing to the $g_e$ values for the $Co^{II}$ ion centers.[33,34] With decreasing temperature, the $\chi_M T$ values for the $Co^{II}$ complexes monotonically decrease, showing a gradual drop below 100 K, which becomes more important as the applied magnetic field increases, as shown in Fig. S23† for **1**. The behavior observed is commonly due to the depopulation of Kramer's excited state levels caused by zero-field splitting (ZFS), in the absence of any close contacts between complexes that might allow for intermolecular exchange interactions.[35]

Field-dependence of the magnetization up to 5 T for **1–3** at 2, 3, 5 and 7 K was also done (Fig. S23†). Magnetization values continuously increase with the applied magnetic field for all the $Co^{II}$ complexes. No complete saturation of the magnetization is observed at 2 K under an applied field of 5 T (2.50 $\mu_B$ for **1**, 5.38 $\mu_B$ for **2** and 2.83 $\mu_B$ for **3**). The observation of non-saturation of magnetization with a high-field indicates the presence of magnetic anisotropy for all the complexes, which is further confirmed by the lack of superposition of the magnetization values in the reduced magnetization plots ($M$ *vs.* $H/T$) between 2–7 K (Fig. S24†).[36] This observation suggests that ZFS is achieved through a slight structural distortion around the $Co^{II}$ ion centers, resulting in a reduction of the three-fold symmetry. By using the PHI software package,[37] an estimation of the anisotropy parameters of **1** and **3** can be obtained from the temperature and field-dependent magnetization data. Because of the presence of two crystallographically independent Co(II) centers, the estimation of the anisotropy parameters for **2** was not considered. By fixing the $g_e$-factor values for the $Co^{II}$ ion centers obtained from the $\chi_M T$ measurements at 300 K (2.71 (1) and 2.81 (3) emu K $mol^{-1}$) in the PHI software, the resulting fit shows positive axial ZFS parameters for all of them ($D$ = 29.05 $cm^{-1}$ and $E$ = 0.82 $cm^{-1}$ for **1**; $D$ = 13.29 $cm^{-1}$ and $E$ = 0.12 $cm^{-1}$ for **3**) (note: fitted curves extracted from PHI can be found in Fig. S25–S28†). This correlates well with the trend observed for the dihedral angles ($\theta$) (91.35(4)° (**1**) < 99.52(5)/80.19(8)° (**2**) < 105.67(7)° (**3**)).

**Dynamic magnetic studies.** To probe the dynamic magnetic behavior of the $Co^{II}$ complexes **1–3**, alternating-current (ac) susceptibility studies were carried out. These measurements were first performed under a zero-dc field (with an oscillating field of 5 Oe) between 2–20 K (Fig. S29†). No out-of-phase signal for the magnetic susceptibility ($\chi_M''$) could be detected in the absence of an applied dc magnetic field at 10 kHz, which was attributed to efficient quantum tunneling of the magnetization (QTM). However, at the same frequency (10 kHz) under a dc applied magnetic field between 0.1–1.1 T, these complexes show a maximum for the temperature-dependence in-phase ($\chi_M'$) and out-of-phase ($\chi_M''$) ac susceptibility between 2–15 K (Fig. S30–S32†). From the analysis of those measurements, to monitor the relaxation process, optimal applied dc magnetic fields of 0.3 (for **1** and **2**) and 0.7 T (for **3**) were selected to suppress quantum tunneling relaxation when performing the temperature and frequency dependence measurements for both $\chi_M'$ and $\chi_M''$ (Fig. 7 and Fig. S33–S35†).

At a minimum, a maximum for the temperature and frequency dependence $\chi_M''$ is observed for all the complexes at these fields, suggesting at least one slow relaxation of the magnetization and a field-induced SIM behavior at low temperatures. It is worth noting that two relaxation processes can be clearly observed for both **1** and **3**. As seen in Fig. 7, the frequency dependence $\chi_M''$ maxima were observed at all temperatures below 5 and 5.75 K for **1** and **3** (for the relaxation processes at higher temperatures in both) and 4.75 K for **2**. Additionally, the observed peaks for the temperature dependence $\chi_M''$ (5.25 K (**1**), 4.75 K (**2**) and 5.75 K (**3**) at 10 kHz) increases in intensity and shift to low temperatures when frequency decreases from 10 kHz to 100 Hz for **1** and **2**, while for **3** decreases in intensity and shift to low temperatures when frequency decreases from 10 kHz to 100 Hz.

Cole–Cole plots were constructed from the $\chi_M'$ and $\chi_M''$ frequency-dependent ac data and fitted using the conventional generalized Debye model with the CC-FIT software package.[38] For **1** and **3** only the relaxation process at higher temperatures was considered for the fitting. The fitted values of $\chi_T$ (isothermal susceptibility), $\chi_S$ (adiabatic susceptibility), $\tau$ and $\alpha$ are summarized in Table S10.† For **1–3**, the curves show typical semicircles at low temperatures (Fig. S36†). A wider range for the distribution of the relaxation time ($\alpha$) values is observed in the low-temperature regime for **1** (0.08–0.24) compared to the distribution of α values found for **2** (0.04–0.15) and **3** (0.05–0.12).

The extracted relaxation times were subsequently used to represent the Arrhenius plot ($\ln \tau$ *vs.* $T^{-1}$) (Fig. 7, green line). To examine the Orbach relaxation process, eqn (1) was employed.

$$\tau^{-1} = {\tau_0}^{-1} \cdot e^{-U_{eff}/K_B T} \quad (1)$$

A fit to the linear portion of the data (at higher temperature values) affords the effective relaxation barriers ($U_{eff}/K_B$) and pre-exponential factors (${\tau_0}^{-1}$) shown in Table S11.† From the trend observed for the experimental data in the $\ln \tau$ *vs.* $T^{-1}$ plot, it can be suggested that more than one relaxation process is involved.

To examine whether other relaxation processes existed, direct (AT) and Raman ($CT^n$), were considered in addition to Orbach (or Arrhenius relaxation) using the following expression and considering that QTM relaxation is suppressed by an applied magnetic field:

$$\tau^{-1} = A \cdot T + C \cdot T^n + {\tau_0}^{-1} \cdot e^{-U_{eff}/K_B T} \quad (2)$$

where $A$ is the coefficient of the direct process, $C$ is the coefficient of the Raman process, and the third term represents the Orbach process.

The best fit parameters obtained for **1–3** are shown in Table 2. The observed values suggest that the primary relaxation processes for all compounds are Raman and Direct processes, as indicated by the minimized residuals. However, Orbach relaxation was also considered as a high-temperature process. Despite investigating both Orbach and Raman relaxation mechanisms, the low $\tau_0$ values and unconventional exponential '$n$' parameters in Raman led us to regard these find-

 

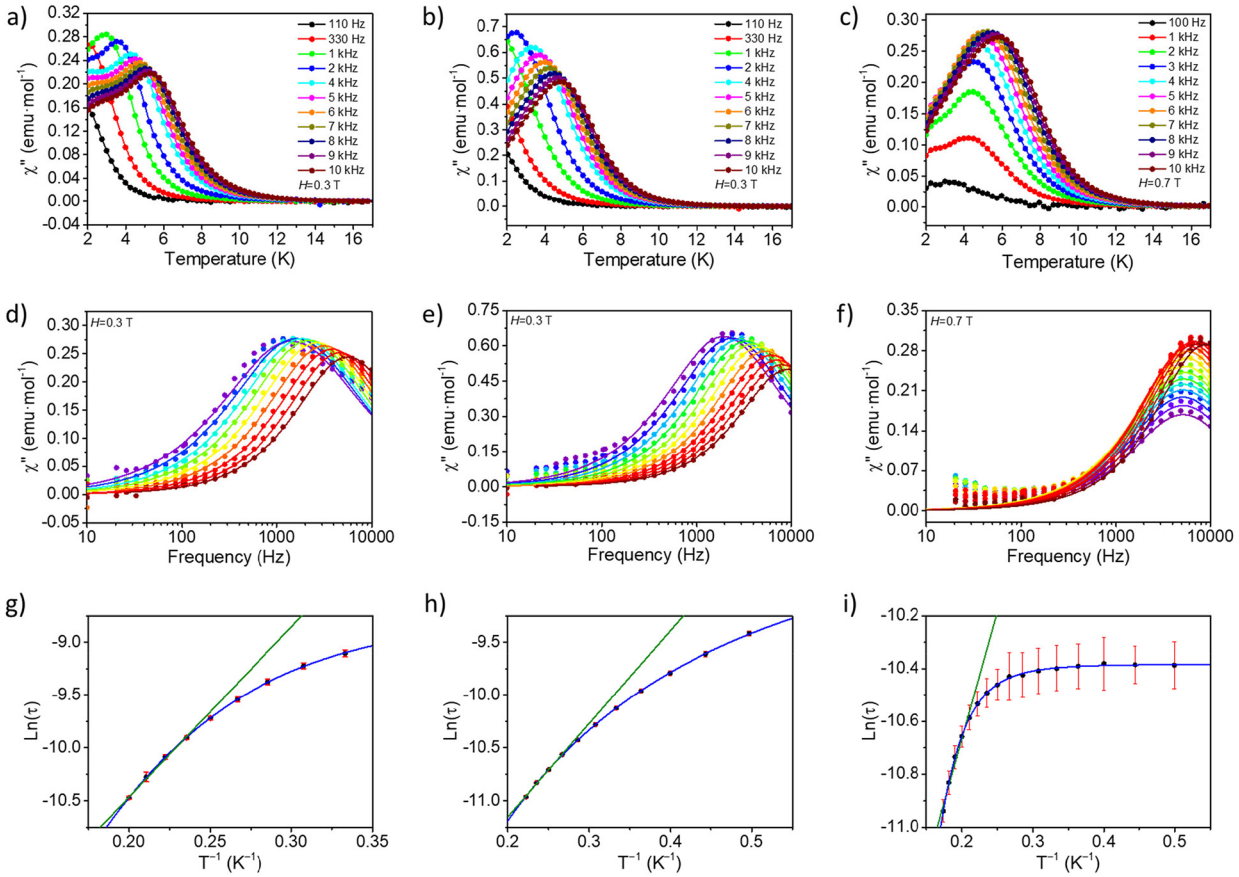


**Fig. 7** Temperature-dependence of the out-of-phase ac susceptibility ($\chi''$) under a dc applied field at different frequencies between 110 to 10 kHz for **1** (a), **2** (b) and **3** (c). Frequency-dependence of the out-of-phase ac susceptibility ($\chi''$) under a dc applied field in the range of 3–5 K for **1** (d), 2–4.75 K for **2** (e), and in the range of 2–5.75 K for **3** (f). Dots corresponds to the experimental data and line correspond to the fitting obtained by CC-FIT software. Note that for **1** and **3** only the relaxation process at higher temperatures was fitted. Arrhenius plots constructed from data for **1** (g), **2** (h) and **3** (i). The solid blue line represents a fit to the two processes simultaneously (Raman and direct), while the green line only to the Orbach process. Error bars (red) are extracted from CC-FIT analysis.

**Table 2** Best fitting parameter of relaxation for **1–3**

| | $H_{applied}$ $(T)$ | $C$ $(s^{-1}\ K^{-n})$ | $n$ | $A$ $(s^{-1}\ K^{-1})$ |
|---|---|---|---|---|
| **1** | 0.3 | 18.69 | 4.57 | $1.64 \times 10^{-4}$ |
| **2** | 0.3 | $1.60 \times 10^{3}$ | 2.33 | $2.38 \times 10^{-4}$ |
| **3** | 0.7 | 0.479 | 6.19 | $3.09 \times 10^{-5}$ |

ings as less significant. Therefore, direct process seems to be predominant at low temperatures for **1–3** and Raman for **2**, which is attributed to low-energy vibrations in the molecular lattice.

Direct mechanism has not been extensively found for $Co^{II}$ octahedral complexes, and although some cases are reported.[39–41] It is important to highlight the complexity of the relaxation process in cobalt systems by covering Orbach process with Raman and Direct processes, this last dominant usually below 3 K. This fact is influenced by the spin entanglement found in Co(II) SIMs.[42] It is also worth mentioning that typical values for $n$ can range from **1–6** (if relaxation mechanism occurs through acoustic or optical phonon interactions), **7** (usually for non-Kramer ions) or **9** (for Kramer ions).[43,44]

## Magneto-structural correlations

Considering the single-crystal X-ray diffraction analysis of **1–3**, together with their magnetic data, several magneto-structural correlations can be inferred. The $\chi_M T$ values obtained for **1–3** confirm that both $^{HOOC}$**Btp** and $^{tBuOOC}$**Btp** exhibit a high-spin configuration for the same coordination number with a structural distortion around the metal as shown in Scheme S1.†[45] In this context, the deviation from an ideal octahedral geometry result in unequally occupied orbitals giving rise to an appreciable magnetic anisotropy. Axial distortions associated to ZFS are obvious when looking at Co–$N_{pyridine}$ distances.

Compounds **1** and **3** clearly have shorter distances for Co–$N_{pyridine}$ bonds (2.1025(14) and 2.0933(14) Å for **1** and 2.0913(14) and 2.0919(14) Å for **3**), indicating a negative axial distortion. Interestingly, higher energy barriers ($U_{eff}/K_B$) are found (16.11 and 9.64 $cm^{-1}$ for **1** and **3**, respectively; Table S11†) for those complexes with positive $D$ values esti-

mated from the static measurements, using the software package PHI, (29.05 $cm^{-1}$ (**1**) and 13.29 $cm^{-1}$ (**3**)). The dominant process for the spin reversal magnetization in **1** and **3** at low temperatures is a direct relaxation process, as shown by the fit of the ln $\tau$ *vs.* $T^{-1}$ plot. This process may be induced by a small rhombic contribution (0.82 $cm^{-1}$ (**1**) and 0.12 $cm^{-1}$ (**3**)), which is in agreement with the largest distortion of the $\varphi$ angle (N1–Co1–N51) from the ideal value of 180° (166 and 169°, respectively). In addition, a large distortion of the octahedral geometry towards a trigonal prismatic environment is observed for both compounds. It is hypothesized this distortion may be triggered by the extent of the π–π interactions between the Btp ligands. Nonetheless, other factors seem to have a large influence in the SIM behavior of these $Co^{II}$ complexes, such as their formal charge caused by the deprotonation of **$^{HOOC}$Btp**, since **3** is the only neutral complex in the series and, therefore, without counterions in their unit cell.

For the case of **2**, a much larger difference between the denoted Co–$N_{pyridine}$ distances for the two crystallographic independent metal complexes in the asymmetric unit (Co1–N1_2 and Co1–N1_1: 2.098(4) and 2.079(4) Å; Co2–N1_3 and Co2–N1_4: 2.099(5) and 2.072(5) Å) is observed, which could be attributed to an unequal negative axial distortion. The energy barrier found in this case is slightly smaller (8.82 $cm^{-1}$, Table S11†). Additionally, the smaller distortion of the $\varphi$ angle (N1_1–Co1–N1_2; N1_3–Co2–N1_4) from the ideal value of 180° (173 and 172°, respectively), gives an idea of the very small rhombic contribution if any.

# Conclusions

Single crystals of three $Co^{II}$ metal complexes comprising two new Btp ligands (**$^{tBuOOC}$Btp** and **$^{HOOC}$Btp**) (**1–3**), were obtained and their structures solved through X-ray diffraction studies. We demonstrate the possibility of tuning the charge of the resulting metal complexes, achieving neutral, monocationic, and dicationic forms, all while preserving the arrangement of the ligand atoms around the metal center that does not change its oxidation state. This control is attained through precise selection of the terminal functionalization for the Btp ligands, and the solvent mixture employed during crystallization.

The crystal structures of all complexes depicted a pseudo-octahedral $CoN_6$ coordination environment around the metal ion, with deviations from ideal octahedral geometry. Static magnetic measurements unveiled significant $\chi_M T$ values, indicating the presence of unquenched orbital angular momentum. Field-dependent magnetization studies confirmed the presence of magnetic anisotropy, while dynamic magnetic studies revealed slow relaxation of magnetization and field-induced single-ion magnet behavior at low temperatures.

From magneto-structural correlations, it is evident that reducing the molecular symmetry increases the anisotropy of the $Co^{II}$ center and, consequently, an increase in the energy barrier would be expected. For instance, the dihedral angle between the ligand planes ($\theta$), which is expected to be 90° in a regular octahedral complex, increases from 91.35° in **1** to 105.67° in **3**. However, the observed energy barriers (Table S11†) follow the order 16.11 $cm^{-1}$ (for **1**) > 9.64 $cm^{-1}$ (for **3**) > 8.82 $cm^{-1}$ (for **2**). From frequency-dependence of the $\chi_M''$ under a dc applied magnetic field (Fig. 5d–f) can be clearly observed that the relaxation of **3** is much faster than that observed for **2** and **3**, and dominated by a temperature-independent process. To explain this, we need to carefully consider both intramolecular factors (such as those promoted by the larger dihedral angle in **3**) and intermolecular interactions, which result from the smaller Co–Co separation in **3** compared to **1** and **2**, leading to increased dipole–dipole interactions. It is important to note that all three compounds display distinct and intricate relaxation processes, which are influenced by both Raman and direct mechanisms, similar to what has been observed in other Co(II) complexes.

In conclusion, understanding the complex interplay between structural distortions and alterations in the secondary coordination sphere is essential for elucidating the factors influencing the single-ion magnetism observed in transition metal coordination compounds. This study highlights the challenges in attributing the observed single-ion magnet behavior to a single factor and emphasizes the need for further research in this field to fully comprehend these intricate relationships.

# Experimental

### General

All chemicals and solvents from commercial sources were used as received. **$^{HOOC}$Btp** and **$^{tBuOOC}$Btp** ligands were synthesized as described below and characterized using HPLC-MS, NMR and MS-ESI-TOF. **CAUTION:** sodium azide and alkyl azides are potentially explosive. The synthesis should be carried out in small quantities and the precursors should be handled with care. Metal complexes **1–3** were obtained using a Schlenk line by the methods described below and subsequently crystallized under a very small constant flow of nitrogen at room temperature. Single crystals of **1–3** were characterized by SCXRD, MS-ESI-TOF, thermogravimetric analysis and CHN elemental analysis. High Resolution Mass spectrometry data were acquired on a Bruker MicrOTOF (ESI-TOF).

### Synthesis of ligands

**Synthesis of 2,6-bis((trimethylsilyl)ethynyl)pyridine (7).** 2.28 g of 2,6-dibromopyridine (9.65 mmol, 1.0 eq.), CuI (37.0 mg, 0.2 mmol, 0.02 eq.), $[PdCl_2(PPh_3)_2]$ (135.0 mg, 0.2 mmol, 0.02 eq.) and 40 mL of triethylamine were added to a 250 mL round bottom flask connected to a Schenk line under $N_2$. While passing a current of $N_2$, trimethylsilylacetylene (2.80 mL, 20.3 mmol, 2.1 eq.) was added to the mixture and the reaction was stirred at room temperature overnight. Then, 50 mL of a saturated solution of $NH_4Cl$ were added and the mixture was stirred for 30 min. The aqueous

 

layer was extracted with $Et_2O$ (3 × 30 mL). The combined organic extract was washed with brine (80 mL), dried with $MgSO_4$, and the solvent removed under vacuum. The residue was purified by flash chromatography (silica gel, hexane : ether, 7 : 3) to afford **7** as a white solid (2.51 g, 96% yield). $^1$H-NMR (500 MHz, $CDCl_3$, $\delta$): 7.55 (t, $^3J$ = 7.8 Hz, 1H), 7.34 (d, $^3J$ = 7.8 Hz, 2H), 0.22 (s, 18H); $^{13}$C-NMR (126 MHz, $CDCl_3$, $\delta$): 143.40 (C), 136.32 (CH), 126.73 (CH), 103.19 (C), 95.46 (C), 0.26 ($CH_3$); DEPT-135 (126 MHz, $CDCl_3$, $\delta$): 136.32 (CH), 126.73 (CH), 0.26 ($CH_3$); MS-ESI: calculated for $[C_{15}H_{22}NSi_2]^+$ 272.13, found 272.17.

**Synthesis of *tert*-butyl 2-azidoacetate (8).** A solution of 5.0 mL of tertbutyl bromoacetate (6.65 g, 34.1 mmol, 1.0 eq.) in 50 mL of DMF was added to a 250 mL round bottom flask connected to a Schenk line under $N_2$ and 11.1 g of $NaN_3$ (170.5 mmol, 5.0 eq.) were then added at room temperature. After stirring the mixture under inert atmosphere for 30 h, 100 mL of water were added, and the crude mixture was extracted with diethyl ether (3 × 40 mL). The combined organic phase was washed with water (2 × 40 mL), 1 M LiCl (2 × 40 mL) and dried over anhydrous $MgSO_4$. The solvent was removed, and the colorless oil was dried under vacuum to give **8** with no further purification (5.04 g, 94% yield). $^1$H-NMR (500 MHz, $CDCl_3$, $\delta$): 3.69 (s, 2H), 1.44 (s, 9H); $^{13}$C-NMR (126 MHz, $CDCl_3$, $\delta$): 167.73 (C), 82.92 (C), 50.86 ($CH_2$), 27.96 ($CH_3$); DEPT-135 (126 MHz, $CDCl_3$, $\delta$): 50.86 ($CH_2$), 27.96 ($CH_3$); IR $\nu_{max}$/cm$^{-1}$ = 2103 ($N_3$), 1738 (C═O).

**Synthesis of $^{tBuOOC}$Btp.** 624.6 mg of **1** (2.3 mmol, 1.0 eq.), $K_2CO_3$ (1.272 g, 9.2 mmol, 4.0 eq.), sodium ascorbate (182.3 mg, 0.98 mmol, 0.4 eq.), $CuSO_4{\cdot}5H_2O$ (69.9 mg, 0.28 mmol, 0.2 eq.), and 903.7 mg of **2** (5.75 mmol, 2.5 eq.) were added to a 100 mL round bottom flask and suspended in a mixture of $CH_3CN : H_2O$ (1 : 1). The mixture was stirred under nitrogen atmosphere for 16 h at room temperature, then a saturated solution of $NH_4Cl$ was added and the mixture was stirred for 30 min. The white solid was isolated by filtration, washed with isopropyl alcohol and deionized water and freeze-dried to give $^{tBuOOC}$**Btp** as a white solid (893.6 mg, 88% yield). $^1$H-NMR (500 MHz, DMSO-$d_6$, $\delta$): 8.67 (s, 2H), 8.00 (s, 3H), 5.39 (s, 4H), 1.46 (s, 18H); $^{13}$C-NMR (126 MHz, DMSO-$d_6$, $\delta$): 116.19 (C), 149.81 (C), 147.06 (C), 138.38 (CH), 124.96 (CH), 118.51 (CH), 82.52 (C), 51.14 ($CH_2$), 27.64 ($CH_3$); DEPT-135 (126 MHz, DMSO-$d_6$, $\delta$): 138.38 (CH), 124.96 (CH), 118.51 (CH), 51.14 ($CH_2$), 27.64 ($CH_3$); MS-ESI: *m*/*z* calculated for $[C_{13}H_{12}N_7O_4]^+$ 442.22, found 442.24.

### Synthesis of $^{HOOC}$Btp

In a 100 mL round bottom flask, containing 513.0 mg of $^{tBuOOC}$**Btp** (1.16 mmol), 5.0 mL of cold TFA were added. The solution was stirred in an ice bath for 1 h, then 70 mL of $Et_2O$ were added dropwise under vigorous stirring and a powdered white solid appeared. The solid was isolated by filtration, washed with $Et_2O$ and deionized water and freeze-dried at −45 °C to afford $^{HOOC}$**Btp** as a white powder. (376.9 mg, 98.5% yield). $^1$H-NMR (500 MHz, DMSO-$d_6$, $\delta$): 13.49 (br, 2H), 8.66 (s, 2H), 7.99 (m, 3H), 5.39 (s, 4H); $^{13}$C-NMR (126 MHz, DMSO-$d_6$, $\delta$): 168.54, 149.85, 147.06, 138.39, 124.96, 118.48, 50.74; DEPT-135 (126 MHz, DMSO-d6, $\delta$): 138.39 (CH), 124.96 (CH), 118.48 (CH), 50,74 ($CH_2$); MS-ESI: *m*/*z* calculated for $[C_{13}H_{12}N_7O_4]^+$ 330.09, found 330.11.

### Synthesis of metal complexes

**Synthesis of $[Co(^{tBuOOC}Btp)_2](ClO_4)_2$ complex (1).** A reaction vessel of 25 mL was charged with 100.0 mg (0.23 mmol, 1.0 eq.) of $^{tBuOOC}$**Btp** and 8 mL of a mixture $CH_3OH : CH_3CN$ (1 : 1). The resultant solution was degassed using Ar before adding the corresponding amount of metallic salt (41.4 mg of $Co(ClO_4)_2{\cdot}6H_2O$, 0.11 mmol, 0.50 eq.) dissolved in 2 mL of the same solvent mixture. The reaction mixture was stirred under Ar atmosphere for 30 minutes and then the solution was transferred to an Erlenmeyer flask and the solvent was left to slowly evaporate under atmospheric pressure at room temperature using a small flow of $N_2$. Clear orange crystals were obtained for **1** (87.8 mg, 68% yield). **(HR)-MS-ESI-TOF**: calculated for $[C_{42}H_{54}ClCoN_{14}O_{12}]$ $[M + ClO_4]^+$ 1041.3066, found 1041.3130; $[C_{42}H_{54}CoN_{14}O_8]$ $[M]^{2+}$ 470.6785, found 470.1592. Elemental analysis found (calculated for $[Co(^{tBuOOC}Btp)_2](ClO_4)_2{\cdot}2CH_3OH$): 43.24(43.54) % for C, 5.41(5.56) % for H and 16.26 (16.45) % for N.

**Synthesis of $[Co(^{HOOC}Btp)(^{OOC}Btp)]ClO_4$ complex (2).** A reaction vessel of 25 mL was charged with 120.0 mg (0.36 mmol, 1.0 eq.) of $^{H}$**Btp** and 13 mL of a mixture $CH_3OH : CH_3CN$ (1 : 1). The resultant suspension was degassed using Ar before adding the corresponding amount of metallic salt (66.7 mg of $Co(ClO_4)_2{\cdot}6H_2O$, 0.18 mmol, 0.50 eq.) dissolved in 2 mL of the same solvent mixture. The reaction mixture was stirred under Ar atmosphere for 30 minutes and then the solution was transferred to an Erlenmeyer flask and the solvent was left to slowly evaporate under atmospheric pressure at room temperature using a small flow of $N_2$. Clear light orange crystals were obtained for $[Co(^{HOOC}Btp)(^{OOC}Btp)]ClO_4{\cdot}3H_2O$ (**2**) (77.2 mg, 49% yield). **(HR)-MS-ESI-TOF**: calculated for $[C_{26}H_{22}ClCoN_{14}O_{12}]$ $[M + H + ClO_4]^+$ 816.0562, found 816.0513; $[C_{26}H_{21}CoN_{14}O_8]$ $[M]^+$ 716.0999, found 716.1102, $[C_{26}H_{22}CoN_{14}O_8]$ $[M + H]^{2+}$ 358.5533, found 358.5598. Elemental analysis found (calculated for $[Co(^{HOOC}Btp)(^{OOC}Btp)]ClO_4{\cdot}3H_2O$): 35.82 (35.90) % for C, 3.25 (3.13) % for H and 22.82 (22.54) % for N.

**Synthesis of $[Co(^{OOC}Btp)_2]$ complex (3).** A reaction vessel of 25 mL was charged with 120.0 mg (0.36 mmol, 1.0 eq.) of $^{HOOC}$**Btp** and 13 mL of a mixture of $H_2O : CH_3CN$ (1 : 1) mixture. The resultant suspension was degassed using Ar before adding the corresponding amount of metallic salt (66.7 mg of $Co(ClO_4)_2{\cdot}6H_2O$, 0.18 mmol, 0.50 eq.) dissolved in 2 mL of the of the same solvent mixture. The reaction mixture was stirred under Ar atmosphere for 30 minutes and then the solution was transferred to an Erlenmeyer flask and the solvent was left to slowly evaporate under atmospheric pressure at room temperature using a small flow of $N_2$. Traslucent orange crystals were obtained for $[Co(^{OOC}Btp)_2]{\cdot}CH_3CN{\cdot}3H_2O$ (**3**) (77.3 mg, 53% yield). **(HR)-MS-ESI-TOF**: calculated for $[C_{26}H_{21}CoN_{14}O_8]$ $[M + H]^+$

716.0999, found 716.1154, $[C_{26}H_{22}CoN_{14}O_8]$ $[M + 2H]^{2+}$ 358.5533, found 358.5468. Elemental analysis found (calculated for $[Co(^{OOC}Btp)_2]\cdot CH_3CN\cdot 3H_2O$): 41.02 (41.49) % for C, 3.50 (3.61) % for H and 26.03 (25.92) % for N.

### SCXRD measurements

Single-crystal X-ray diffraction was measured on a Bruker D8 Venture Photon III C14 κ – geometry diffractometer system equipped with an Incoatec high brillance IμS 3.0 microsource (MoKα, $\lambda$ = 0.71073 Å). Crystallographic data for all the complexes were deposited in the Cambridge Structural Database (CSD) with the following deposit numbers: CCDC 2281065 for **1**; CCDC 2281066 for **2**; CCDC 2281061 for **3**.†

### Magnetic measurements

All magnetic measurements were performed solely on polycrystalline samples composed of ground single crystals packed on a plastic capsule using a Quantum Design MPMS-XL-5 SQUID magnetometer and a Quantum Design PPMS-5 both equipped with a 5 T magnet. After magnetic measurements powder X-ray diffraction measurements performed at the ground single crystals (compound **1** and **2**) show no evidence of grinding causing structural changes on the compounds (Fig. S37†). Comparison with the simulated data from single-crystal X-ray diffraction measurements taken at 100 K suggests that the additional small peaks observed may be attributed to slight desolvation or the presence of a very minor impurity. Diamagnetic corrections were applied using tabulated Pascal constants. Small diamagnetic contribution from the plastic capsule was also considered. Variable-temperature susceptibility experiments were carried out in the temperature range 2–400 K under a static magnetic field of 0.1 and 1 T. Field-dependence magnetization measurements up to 5 T were performed at different temperatures between 2–7 K. At low temperatures ac susceptibility data were recorded with an oscillating field of 3.95 G amplitude at frequencies between 0.1 and 10 kHz. The optimum static fields for ac measurements were determined by measuring the frequency dependence of the in-phase and out-of-phase component of the susceptibility at 10 kHz under the application of dc fields ranging from 0 to 1.1 T.

## Author contributions

GRM designed the synthetic route and synthetized the ligand with the assistance of MOC and DSB; GRM and DSB performed the spectroscopic titrations; GRM and DSB calculate the association constants of the metal complexes; MOC and DSB prepared the metal complexes and isolate the single crystals; ALLS performed the single crystal X-Ray diffraction experiments and solved and refined the structures; EPQD, MOC and MCGL analyzed the crystal structures; MCGL, YSA and MOC analyzed the magnetic data; MCGL carried out the conceptualization and magneto-structural correlations. MEV designed the ligand, supervised the spectroscopic data fit and reviewed the manuscript draft together with MVL; MCGL, MEV and MVL funding acquisition; GRM, MOC and YSA writing-original draft preparation. MCGL writing-reviewing and editing the final manuscript. All authors commented on draft versions and approved the final version.

## Data availability

The data supporting this article have been included as part of the ESI.† Crystallographic data for compound **1–3** have been deposited at the Cambridge Structural Database (CSD) with the following deposit numbers: CCDC 2281065 for **1**; CCDC 2281066 for **2**; CCDC 2281061 for **3** and can be obtained from **https://www.ccdc.cam.ac.uk/structures/?**

## Conflicts of interest

There are no conflicts to declare.

## Acknowledgements

GRM, MOC and EPQD thanks Xunta de Galicia for postdoctoral (grant 2018-PG020) and predoctoral (ED481A-2019/210 and ED481-2020/155) fellowships. YSA, GRM, MOC, EPQD and MCGL acknowledge financial support from European Research Council through the ERC-STG (NANOCOMP-679124). MCGL, MVL and MEV thank the Xunta de Galicia (grant ED431C 2021/29; ED431C 2024/05, the Oportunius Program (GAIN)) for financial support. MVL thanks Ideas Semilla 2021 – IDEAS211154VÁZQ for financial support. MVL, MEV and MCGL thank grants CNS2023-145421, PID2021-127341OB-I00, PID2021-127857NB-I00, PID2021-127702NB-I00 and TED2021-131451BC21 funded by MCIN/AEI/10.13039/501100011033 and by ERDF A way of making Europe. MCGL acknowledges financial support from the Ministry of Science of Spain (RYC-2016-20258). Authors thank J. M. Martínez-Agudo for technical assistance in the magnetic data acquisition.

## References

1 M. Feng and M.-L. Tong, Single Ion Magnets from 3d to 5f: Developments and Strategies, *Chem. – Eur. J.*, 2018, **24**, 7574–7594.
2 M. Mannini, F. Pineider, P. Sainctavit, C. Danieli, E. Otero, C. Sciancalepore, A. M. Talarico, M. A. Arrio, A. Cornia, D. Gatteschi and R. Sessoli, Magnetic memory of a single-molecule quantum magnet wired to a gold surface, *Nat. Mater.*, 2009, **8**, 194–197.
3 K. S. Pedersen, A.-M. Ariciu, S. McAdams, H. Weihe, J. Bendix, F. Tuna and S. Piligkos, Toward Molecular 4f Single-Ion Magnet Qubits, *J. Am. Chem. Soc.*, 2016, **138**, 5801–5804.

4 A. R. Rocha, V. M. García-Suárez, S. W. Bailey, C. J. Lambert, J. Ferrer and S. Sanvito, Towards Molecular Spintronics, *Nat. Mater.*, 2005, **4**, 335–339.

5 (*a*) D. N. Woodruff, R. E. Winpenny and R. A. Layfield, Lanthanide Single-Molecule Magnets, *Chem. Rev.*, 2013, **113**, 5110–5148; (*b*) S. G. McAdams, A.-M. Ariciu, A. K. Kostopoulos, J. P. S. Walsh and F. Tuna, Molecular single-ion magnets based on lanthanides and actinides: Design considerations and new advances in the context of quantum technologies, *Coord. Chem. Rev.*, 2017, **346**, 216–239.

6 (*a*) Y. Rechkemmer, F. D. Breitgoff, M. Van der Meer, M. Atanasov, M. Hakl, M. Orlita, P. Neugebauer, F. Neese, B. Sarkar and J. Van Slageren, A four-coordinate cobalt(II) single-ion magnet with coercivity and a very high energy barrier, *Nat. Commun.*, 2016, **7**, 10467; (*b*) P. C. Bunting, M. Atanasov, E. Damgaard-Møller, M. Perfetti, I. Crassee, M. Orlita, J. Overgaard, J. Van Slageren, F. Neese and J. R. Long, *Science*, 2018, **362**, 7319.

7 X.-N. Yao, J.-Z. Du, Y.-Q. Zhang, X.-B. Leng, M.-W. Yang, S.-D. Jiang, Z.-X. Wang, Z.-W. Ouyang, L. Deng, B.-W. Wang and S. Gao, Two-Coordinate Co(II) Imido Complexes as Outstanding Single-Molecule Magnets, *J. Am. Chem. Soc.*, 2017, **139**, 373–380.

8 J. Martí-Rujas and F. Guo, Dehydrohalogenation reactions in second-sphere coordination complexes, *Dalton Trans.*, 2021, **50**, 11665–11680.

9 L. R. Widger, C. G. Davies, T. Yang, M. A. Siegler, O. Troeppner, G. N. L. Jameson, I. Ivanović-Burmazović and D. P. Goldberg, Dramatically Accelerated Selective Oxygen-Atom Transfer by a Nonheme Iron(IV)-Oxo Complex: Tuning of the First and Second Coordination Spheres, *J. Am. Chem. Soc.*, 2014, **136**, 2699–2702.

10 (*a*) V. Jornet-Mollá, Y. Duan, C. Giménez-Saiz, Y. Tang, P. Li, F. M. Romero and R. Xiong, A Ferroelectric Iron(II) Spin Crossover Material, *Angew. Chem.*, 2017, **129**, 14240–14244; (*b*) M. C. Giménez-López, M. Clemente-León and C. Giménez-Saiz, Unravelling the spin-state of solvated [Fe(bpp)2]$^{2+}$ spin-crossover complexes: structure–function relationship, *Dalton Trans.*, 2018, **47**, 10453–10462.

11 (*a*) W. Phonsri, P. Harding, L. Liu, S. G. Telfer, K. S. Murray, B. Moubaraki, T. M. Ross, G. N. L. Jameson and D. J. Harding, Solvent modified spin crossover in an iron (III) complex: phase changes and an exceptionally wide hysteresis, *Chem. Sci.*, 2017, **8**, 3949–3959; (*b*) A. Galet, A. B. Gaspar, M. C. Muñoz and J. A. Real, Influence of the Counterion and the Solvent Molecules in the Spin Crossover System $[Co(4\text{-terpyridone})_2]X_p{\cdot}nH_2O$, *Inorg. Chem.*, 2006, **45**, 4413–4422.

12 (*a*) R. Herchel, P. Zoufalý and I. Nemec, The effect of the second coordination sphere on the magnetism of $[Ln(NO_3)_3(H_2O)_3]\cdot$ (18-crown-6) (Ln = Dy and Er), *RSC Adv.*, 2019, **9**, 569–575; (*b*) J. Jung, O. Cador, K. Bernot, F. Pointillart, J. Luzon and B. L. Guennic, Influence of the supramolecular architecture on the magnetic properties of a DyIII single-molecule magnet: an ab initio investigation, *Beilstein J. Nanotechnol.*, 2014, **5**, 2267–2274; (*c*) Z.-B. Hu, Z.-Y. Jing, M.-M. Li, L. Yin, Y.-D. Gao, F. Yu, T.-P. Hu, Z. Wang and Y. Song, Important Role of Intermolecular Interaction in Cobalt(II) Single-Ion Magnet from Single Slow Relaxation to Double Slow Relaxation, *Inorg. Chem.*, 2018, **57**, 10761–10767.

13 D. A. Reed, T. J. Hochuli, N. A. Gadjieva, S. He, R. A. Wiscons, A. K. Bartholomew, A. M. Champsaur, M. L. Steigerwald, X. Roy and C. Nuckolls, Controlling Ligand Coordination Spheres and Cluster Fusion in Superatoms, *J. Am. Chem. Soc.*, 2022, **144**, 306–313.

14 M. Ostermeier, M.-A. Berlin, R. M. Meudtner, S. Demeshko, F. Meyer, C. Limberg and S. Hecht, Complexes of Click-Derived Bistriazolylpyridines: Remarkable Electronic Influence of Remote Substituents on Thermodynamic Stability as well as Electronic and Magnetic Properties, *Chem. – Eur. J.*, 2010, **16**, 10202–10213.

15 J. P. Byrne, J. A. Kitchen and T. Gunnlaugsson, The btp [2,6-bis(1,2,3-triazol-4-yl)pyridine] binding motif: a new versatile terdentate ligand for supramolecular and coordination chemistry, *Chem. Soc. Rev.*, 2014, **43**, 5302–5325.

16 I. Capel Berdiell, D. J. Davies, J. Woodworth, R. Kulmaczewski, O. Cespedes and M. A. Halcrow, Structures and Spin States of Iron(II) Complexes of Isomeric 2,6-Di(1,2,3-triazolyl)pyridine Ligands, *Inorg. Chem.*, 2021, **60**, 14988–15000.

17 M. A. Palacios, I. F. Díaz-Ortega, H. Nojiri, E. A. Suturina, M. Ozerov, J. Krzystek and E. Colacio, Tuning magnetic anisotropy by the π-bonding features of the axial ligands and the electronic effects of gold(I) atoms in 2D $\{Co(L)_2[Au(CN)_2]_2\}_n$ metal–organic frameworks with field-induced single-ion magnet behaviour, *Inorg. Chem. Front.*, 2020, **7**, 4611–4630.

18 Z.-Y. Ding, Y.-S. Meng, Y. Xiao, Y.-Q. Zhang, Y.-Y. Zhu and S. Gao, Probing the influence of molecular symmetry on the magnetic anisotropy of octahedral cobalt(II) complexes, *Inorg. Chem. Front.*, 2017, **4**, 1909–1916.

19 (*a*) Q. V. C. van Hilst, N. R. Lagesse, D. Preston and J. D. Crowley, Functional metal complexes from CuAAC "click" bidentate and tridentate pyridyl-1,2,3-triazole ligands, *Dalton Trans.*, 2017, **47**, 997–1002; (*b*) E. P. McCarney, C. S. Hawes, J. A. Kitchen, K. Byrne, W. Schmitt and T. Gunnlaugsson, A Lanthanide Luminescent Cation Exchange Material Derived from a Flexible Tricarboxylic Acid 2,6-Bis(1,2,3-triazol-4-yl)pyridine (btp) Tecton, *Inorg. Chem.*, 2018, **57**, 3920–3930; (*c*) R. A. S. Vasdev, D. Preston and J. D. Crowley, Functional metallosupramolecular architectures using 1,2,3-triazole ligands: it's as easy as 1,2,3 "click", *Dalton Trans.*, 2017, **46**, 2402–2414.

20 (*a*) Q. V. C. van Hilst, N. R. Lagesse, D. Preston and J. D. Crowley, Functional metal complexes from CuAAC "click" bidentate and tridentate pyridyl-1,2,3-triazole ligands, *Dalton Trans.*, 2017, **47**, 997–1002; (*b*) Y. Li, J. C. Huffman and A. H. Flood, Can terdentate 2,6-bis(1,2,3-triazol-4-yl)pyridines form stable coordination compounds?, *Chem. Commun.*, 2007, 2692–2694.

21 (*a*) E. P. McCarney, J. I. Lovitt and T. Gunnlaugsson, Mechanically Interlocked Chiral Self-Templated [2] Catenanes from 2,6-Bis(1,2,3-triazol-4-yl)pyridine (btp) Ligands, *Chem. – Eur. J.*, 2021, **27**, 12052–12057; (*b*) L. Xu, Y. Li and Y. Li, Application of "Click" Chemistry to the Construction of Supramolecular Functional Systems, *Asian J. Org. Chem.*, 2014, **3**, 582–602; (*c*) D. A. W. Ross, J. A. Findlay, R. A. S. Vasdev and J. D. Crowley, Can 2-Pyridyl-1,2,3-triazole "Click" Ligands be Used to Develop Cu(I)/Cu(II) Molecular Switches?, *ACS Omega*, 2021, **6**, 30115–30129.

22 (*a*) P. Kuzmič, Program DYNAFIT for the analysis of enzyme kinetic data: application to HIV proteinase, *Anal. Biochem.*, 1996, **237**, 260–273; (*b*) P. Kuzmič, DynaFit–a software package for enzymology, *Methods Enzymol.*, 2009, **467**, 247–280.

23 J. Gómez-González, Y. Pérez, G. Sciortino, L. Roldan-Martín, J. Martínez-Costas, J. Maréchal, I. Alfonso, M. Vázquez López and M. E. Vázquez, Dynamic Stereoselection of Peptide Helicates and Their Selective Labeling of DNA Replication Foci in Cells, *Angew. Chem., Int. Ed.*, 2021, **60**, 8859–8866.

24 J. Gómez-González, D. Bouzada, L. A. Pérez-Márquez, G. Sciortino, J.-D. Maréchal, M. Vázquez López and M. E. Vázquez, Stereoselective Self-Assembly of DNA Binding Helicates Directed by the Viral β-Annulus Trimeric Peptide Motif, *Bioconjugate Chem.*, 2021, **32**, 1564–1569.

25 R. Shunmugam, G. J. Gabriel, K. A. Aamer and G. N. Tew, Metal-Ligand-Containing Polymers: Terpyridine as the Supramolecular Unit, *Macromol. Rapid Commun.*, 2010, **31**, 784–793.

26 A. Winter, M. Gottschaldt, G. R. Newkome and U. S. Schubert, Terpyridines and their Complexes with First Row Transition Metal Ions:Cytotoxicity, Nuclease Activity and Self-Assembly of Biomacromolecules, *Curr. Top. Med. Chem.*, 2012, **12**, 158–175.

27 A. L. Spek, PLATON SQUEEZE: a tool for the calculation of the disordered solvent contribution to the calculated structure factors, *Acta Crystallogr., Sect. C: Struct. Chem.*, 2015, **C71**, 9–18.

28 (*a*) J. Vallejo, F. R. Fortea-Perez, E. Pardo, S. Benmansour, I. Castro, J. Krzystek, D. Armentano and J. Cano, Guest-dependent single-ion magnet behaviour in a cobalt(II) metal-organic framework., *Chem. Sci.*, 2016, **7**, 2286–2293; (*b*) V. Garcia-Lopez, F. J. Orts-Mula, M. Palacios-Corella, J. M. Clemente-Juan, M. Clemente-Leon and E. Coronado, Field-induced slow relaxation of magnetization in a mononuclear Co(II) complex of 2,6-bis(pyrazol-1-yl)pyridine functionalized with a carboxylic acid, *Polyhedron*, 2018, **150**, 54–60.

29 (*a*) M. B.-L. Cointe, J. Hébert, C. Baldé, N. Moisan, L. Toupet, P. Guionneau, J. F. Létard, E. Freysz, H. Cailleau and E. Collet, Intermolecular control of thermoswitching and photoswitching phenomena in two spin-crossover polymorphs, *Phys. Rev. B: Condens. Matter Mater. Phys.*, 2012, **85**, 064114; (*b*) J. A. Alonso, M. J. Martínez-Lopez, M. T. Casais and M. T. Fernández-Díaz, Evolution of the Jahn–Teller Distortion of $MnO_6$ Octahedra in $RMnO_3$ Perovskites (R = Pr, Nd, Dy, Tb, Ho, Er, Y): A Neutron Diffraction Study, *Inorg. Chem.*, 2000, **39**, 917–923; (*c*) M. Marchivie, P. Guionneau, J.-F. Létard and D. Chasseau, Photo-induced spin-transition: the role of the iron(II) environment distortion, *Acta Crystallogr., Sect. B: Struct. Sci.*, 2005, **61**, 25–28.

30 M. A. Halcrow, Structure:function relationships in molecular spin-crossover complexes, *Chem. Soc. Rev.*, 2011, **40**, 4119–4142.

31 J. K. McCusker, A. L. Rheingold and D. N. Hendrickson, Variable-Temperature Studies of Laser-Initiated $^5T_2 \rightarrow {}^1A1$ Intersystem Crossing in Spin-Crossover Complexes: Empirical Correlations between Activation Parameters and Ligand Structure in a Series of Polypyridyl Ferrous Complexes, *Inorg. Chem.*, 1996, **35**, 2100–2112.

32 C. Janiak, A critical account on Π–Π stacking in metal complexes with aromatic nitrogen-containing ligands, *J. Chem. Soc., Dalton Trans.*, 2000, 3885–3896.

33 V. García-López, F. J. Orts-Mula, M. Palacios-Corella, J. M. Clemente-Juan, M. Clemente-León and E. Coronado, Field-induced slow relaxation of magnetization in a mononuclear Co(II) complex of 2,6-bis(pyrazol-1-yl)pyridine functionalized with a carboxylic acid, *Polyhedron*, 2018, **150**, 54–60.

34 F. E. Mabbs, D. J. David and J. Machin, *Magnetism and transition metal complexes*, Dover Publications, 2008.

35 R. Boča, Zero-field splitting in metal complexes, *Coord. Chem. Rev.*, 2004, **248**, 757–815.

36 Y. Cui, Y. Xu, X. Liu, Y. Li, B. L. Wang, Y. Dong, W. Li and S. Lei, Field-Induced Single-Ion Magnetic Behavior in Two Mononuclear Cobalt(II) Complexes, *Chem. – Asian J.*, 2019, **14**, 2620–2628.

37 N. F. Chilton, R. P. Anderson, L. D. Turner, A. Soncini and K. S. Murray, PHI: A powerful new program for the analysis of anisotropic monomeric and exchange-coupled polynuclear d- and f-block complexes, *J. Comput. Chem.*, 2013, **34**, 1164–1175.

38 D. Reta and N. F. Chilton, Uncertainty estimates for magnetic relaxation times and magnetic relaxation parameters, *Phys. Chem. Chem. Phys.*, 2019, **21**, 23567–23575.

39 H. Zenno, F. Kobayashi, M. Nakamura, Y. Sekine, L. F. Lindoy and S. Hayami, Hydrogen bond-induced abrupt spin crossover behaviour in 1-D cobalt(II) complexes – the key role of solvate water molecules, *Dalton Trans.*, 2021, **50**, 7843–7853.

40 N. Portolés-Gil, S. Gómez-Coca, O. Vallcorba, G. Marbán, N. Aliaga-Alcalde, A. López-Periago, J. A. Ayllón and C. Domingo, Single molecule magnets of cobalt and zinc homo- and heterometallic coordination polymers prepared by a one-step synthetic procedure, *RSC Adv.*, 2020, **10**, 45090–45104.

41 Q. Yang, G.-L. Wang, Y.-Q. Zhang and J. Tang, Self-assembly of fish-bone and grid-like CoII-based single-molecule

 

magnets using dihydrazone ligands with NNN and NNO pockets, *Dalton Trans.*, 2022, **51**, 13928–13937.

42 S. Gómez-Coca, A. Urtizberea, E. Cremades, P. J. Alonso, A. Camón, E. Ruiz and F. Luis, Origin of slow magnetic relaxation in Kramers ions with non-uniaxial anisotropy, *Nat. Commun.*, 2014, **5**, 1–8.

43 K. N. Shrivastava, Theory of Spin–Lattice Relaxation, *Phys. Status Solidi.*, 1983, **117**, 437–458.

44 A. Singh and K. N. Shrivastava, Optical-acoustic two-phonon relaxation in spin systems, *Phys. Status Solidi*, 1979, **95**, 273–277.

45 (*a*) P. Gütlich, H. A. Goodwin and H. A. Goodwin, Recent Advances of Spin Crossover Research, *Top. Curr. Chem.*, 2004, 23–47; (*b*) R. Hogg and R. G. Wilkins, Exchange studies of certain chelate compounds of the transitional metals. Part VIII. 2,2′,2″-terpyridine complexes, *J. Chem. Soc.*, 1962, 341–350; (*c*) S. Klokishner and S. M. Ostrovsky, Exchange studies of certain chelate compounds of the transitional metals. Part VIII. 2,2′,2″-terpyridine complexes Interplay of Jahn-Teller Ordering and Spin Crossover in Co(II) Compounds, *Magnetochemistry*, 2020, **6**, 62–73.